

Braiding higher-order Majorana corner states through their spin degree of freedom

Xiao-Hong Pan,^{1,2} Xun-Jiang Luo,^{1,2} Jin-Hua Gao,^{1,2,*} and Xin Liu^{1,2,†}

¹*School of Physics and Institute for Quantum Science and Engineering, Huazhong University of Science and Technology, Wuhan, Hubei 430074, China*

²*Wuhan National High Magnetic Field Center and Hubei Key Laboratory of Gravitation and Quantum Physics, Wuhan, Hubei 430074, China*

(Dated: November 25, 2021)

In this work, we study the spin texture of a class of higher-order topological superconductors (HOTSC) and show how it can be used to detect and braid Majorana corner modes (MCMs). This class of HOTSC is composed of two-dimensional topological insulators with s-wave superconductivity and in-plane magnetic fields, which offers advantages in experimental implementation. The spin polarization of the MCMs in this class is perpendicular with the applied magnetic field direction and is opposite on intrinsic orbitals, resulting in an overall ferrimagnetic spin texture. As a result, we find that the spin-selective Andreev reflection can be observed in a transverse instead of parallel direction to the applied magnetic field. Meanwhile, this spin texture leads to the gate-tunable 4π periodic ϕ_0 Josephson current that performs qualitatively different behavior from the topologically trivial ϕ_0 -junction under rotating the in-plane magnetic field. Meanwhile, the existence of the MCMs in this class does not depend on the in-plane magnetic field direction. This gives rise to great advantage in constructing all electronically controlled Majorana network for braiding, which is confirmed through our numerical simulation. We thus provide a comprehensive scheme for probing non-Abelian statistics in this class of HOTSCs.

The braiding of Majorana zero modes (MZMs) is crucial for revealing their non-Abelian braiding statistics and implementing topological quantum computing (TQC)[1–7]. In particular, it is now widely accepted that the zero-bias conductance peak (ZBCP) alone is insufficient to confirm the existence of MZM[8–14]. Only the observation of non-Abelian braiding statistics is the most conclusive proof of their existence. Therefore, an experimentally feasible braiding and reading scheme is necessary for any promising Majorana platform. Meanwhile, the MZM wave function is fully spin-polarized [15–19], resulting in universal spin-triplet superconducting correlation [20–24]. Accordingly, these spin properties can cause spin-dependent transport phenomena such as spin-selective Andreev reflection and topological ϕ_0 -junction [16, 17, 25–30], which can serve as the evidence of MZMs beyond the ZBCP. Remarkably, the latter comes from the spin-dependent Josephson coupling, which is not only useful in measuring the fermion-parity of two MZMs fusion but also essential to implement the MZMs braiding [5, 27, 31–34]. Although the spin properties of Majorana zero-energy modes can provide a significant route for their detection and braiding, their studies have primarily focused on first-order TSCs[34, 35]. Recent studies on higher-order topological superconductors (HOTSCs) have opened up a new perspective: directly implementing MZMs on corners of two-dimensional (2D) or three-dimensional (3D) systems[36–63]. This not only provides a new topological phase but also has advantages for MZM experimental realization. Although many works have provided rich proposals for the realization of HOTSC, the braiding scheme of MZMs in HOTSC has not been well investigated.

In this work, we study the spin texture of Majorana

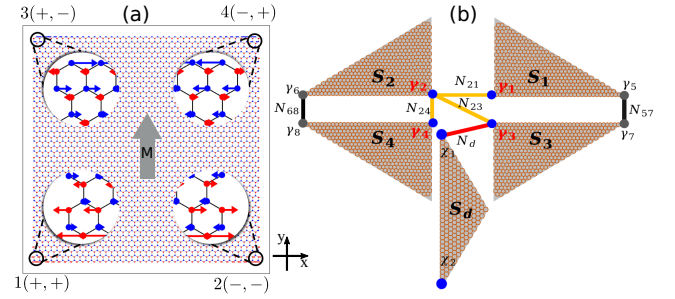


FIG. 1. (a) By fixing magnetic field along $+y$, the spin polarization distribution of MCMs in bismuthene when the system preserve chiral symmetry at parameters according to Ref.[64]. (b) are HOTSCs. The MCMs $\gamma_{1,2,3,4}$, $\chi_{1,2}$ sit on the HOTSC $S_{1,2,3,4,d}$. N_{21} , N_{23} , N_{24} are the normal wires to control the MCMs coupling. The MCMs $\gamma_{5,6,7,8}$ remain coupled through the wires N_{57} and N_{68} in the whole process. N_d is the normal wire connecting γ_3 and χ_1 which are used to detect the braiding result.

corner modes (MCM) in a class of HOTSC and show how it bring advantages in detection as well as implementation of braiding MCMs. The HOTSC is made up of a two-dimensional topological insulator [64–66], an s-wave superconductor, and an in-plane magnetic field, all of which are experimentally feasible. In the case that the system has well-defined chiral symmetry, we found that this class of HOTSC supports the MCMs whose spin direction is perpendicular to the magnetic field direction (Fig. 1(a)). As a result, the spin-selective Andreev reflection can be observed in a transverse direction to the applied magnetic field. Remarkably, this spin texture leads to the anomalous 4π periodic ϕ_0 Josephson current that performs qualitatively different from the topologi-

cally trivial ϕ_0 -junction. This is not only useful for detecting MCMs but also required for the implementation of all electrically controllable Majorana braiding. Meanwhile, the existence of MCMs in the class of HOTSC we study is independent on the in-plane magnetic field direction[48]. This not only provides additional parameter space to distinguish the MCMs from trivial states but also bring significant advantages in the construction of the Majorana network (Fig. 1(b)). Based on this network, we provide a comprehensive scheme for braiding MCMs and probing their non-Abelian statistics in HOTSCs through topological ϕ_0 -junction.

Spin texture of MCMs - The class of HOTSC we study can be generally described by a minimal Hamiltonian [48, 53, 55, 56]

$$H(k) = d_1(k)\tau_z s_0 \sigma_x + d_2(k)\tau_z s_0 \sigma_y + d_3(k)\tau_0 s_z \sigma_z + M(\cos \theta \tau_z s_x + \sin \theta \tau_0 s_y) \sigma_0 + \Delta \tau_y s_y \sigma_0, \quad (1)$$

where the first three terms give the Hamiltonian of 2D TI with $d_{i=1,2,3}(k)$ depending on the specific models, such as Kane-Mele [67, 68] and Bernevig-Hughes-Zhang models [69, 70], Pauli matrices τ , s and σ act on the Nambu, spin and orbital [71] space respectively, M and Δ_{sc} are magnitude of Zeeman splitting and s-wave pairing, respectively, and θ is the polar angle in the x-y plane indicating the direction of magnetic field. It has been shown in several works that the existence of MCMs does not depend on the in-plane magnetic field direction[48]. For simplicity and without loss of generality, we first take the magnetic field along y direction. The Hamiltonian of Eq. (1) possess two chiral symmetry[71], and the operator in this case take the form

$$\mathcal{C}_1 = \tau_0 s_x \sigma_z \quad \text{and} \quad \mathcal{C}_2 = \tau_y s_x \sigma_0. \quad (2)$$

The two chiral symmetry operators commute with each other and are block diagonal in orbital space. Therefore we can classify their eight common eigen-basis $\Phi_{(\epsilon_1, \epsilon_2)}^\lambda$ into two categories according to λ which is the eigenvalues of σ_z in Tab. I.

TABLE I. Eigen-basis of chiral operators.

$(\epsilon_1, \epsilon_2) \backslash \lambda$	+	-
(+, +)	$ \tau_y = +1\rangle \otimes \rightarrow\rangle$	$ \tau_y = -1\rangle \otimes \leftarrow\rangle$
(+, -)	$ \tau_y = -1\rangle \otimes \rightarrow\rangle$	$ \tau_y = +1\rangle \otimes \leftarrow\rangle$
(-, -)	$ \tau_y = +1\rangle \otimes \leftarrow\rangle$	$ \tau_y = -1\rangle \otimes \rightarrow\rangle$
(-, +)	$ \tau_y = -1\rangle \otimes \leftarrow\rangle$	$ \tau_y = +1\rangle \otimes \rightarrow\rangle$

Here, ϵ_1 and ϵ_2 are the eigenvalues of \mathcal{C}_1 and \mathcal{C}_2 respectively and \rightarrow (\leftarrow) indicates the spin along positive (negative) x direction. Due to the chiral symmetry, the MCMs must be the eigenstates of the chiral operators. Consequently, each MCM can be labeled by the eigenvalues (ϵ_1, ϵ_2) . We note that the system also has effective mirror symmetry $\hat{M}_x H(k_x, k_y) \hat{M}_x^{-1} = H(-k_x, k_y)$ and

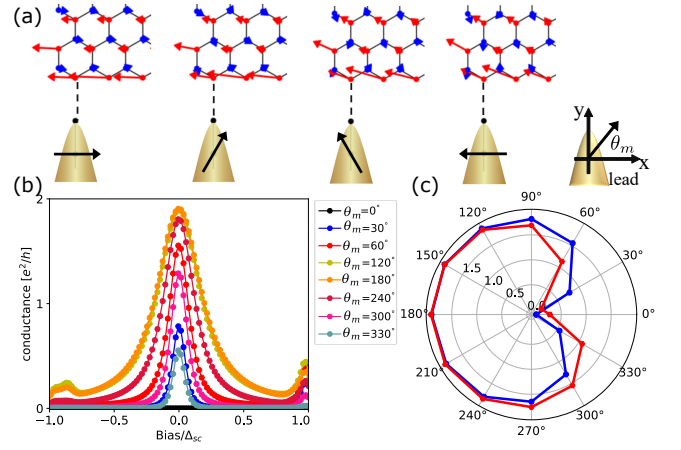


FIG. 2. The fixed magnetic field is along the $+y$ direction. (a). From left to right are the spin textures of the MCM at γ_I for lead polarizations along 0° , 60° , 120° and 180° , while the system possess chiral symmetry. (b) is the conductance of MCMs at γ_I at $k_B T = 0.03 \Delta_{sc}$. (c) The blue and red curves represent the relationship between the polarization direction and the height of zero bias conductance, respectively. In order to reduce the computational effort, we mainly perform numerical calculations in low energy space of bismuthene model.

$\hat{M}_y H(k_x, k_y) \hat{M}_y^{-1} = H(k_x, -k_y)$ with $\hat{M}_x = i\tau_0 \sigma_0 s_y$ and $\hat{M}_y = -i\tau_0 \sigma_x s_y$ respectively. The product of these two effective mirror operators, $\hat{I} = \hat{M}_x \hat{M}_y = \tau_0 \sigma_x \sigma_0$, gives the inversion operator $\hat{I} H(k_x, k_y) \hat{I}^{-1} = H(-k_x, -k_y)$. Without loss of generality, we take the MCM at corner 1 (Fig. 1(a)) to has eigenvalues of the chiral operators (+, +) as

$$\Psi_1(x, y) = \alpha(x, y) \Phi_{(+,+)}^+ + \beta(x, y) \Phi_{(+,+)}^-, \quad (3)$$

where $\alpha(x, y)$ and $\beta(x, y)$ provide the spatial distribution of the wave function. Then, the MCMs localized at other corners can be obtained as

$$(\Psi_2, \Psi_3, \Psi_4) = (\hat{M}_x, \hat{M}_y, \hat{I}) \Psi_1. \quad (4)$$

Note that the spin polarization in the eight-basis is perpendicular to the magnetic field. This is very different from the spin polarization of MZMs in the semiconductor nanowire and vortex core, which is parallel with the magnetic field direction. To study the physical property of this spin texture, thereafter, we take the 2DTI to be bismuthene which has been experimentally observed with topological non-trivial band gap of 0.5eV[64–66]. The spin polarization of each MCMs is numerically calculated and plot in Fig. 1(a), in which the four MCMs $\gamma_{i=1,2,3,4}$ is consistent with our symmetry analysis. Here the $\lambda = +1$ and $\lambda = -1$ refer to the A (blue) and B (red) sublattice of honeycomb lattice (Fig. 1(a)). The above symmetry analysis can be applied to arbitrary in-plane magnetic field direction [71].

Transverse spin-selective tunneling - The spin texture of the MCMs can be observed through observing the spin-

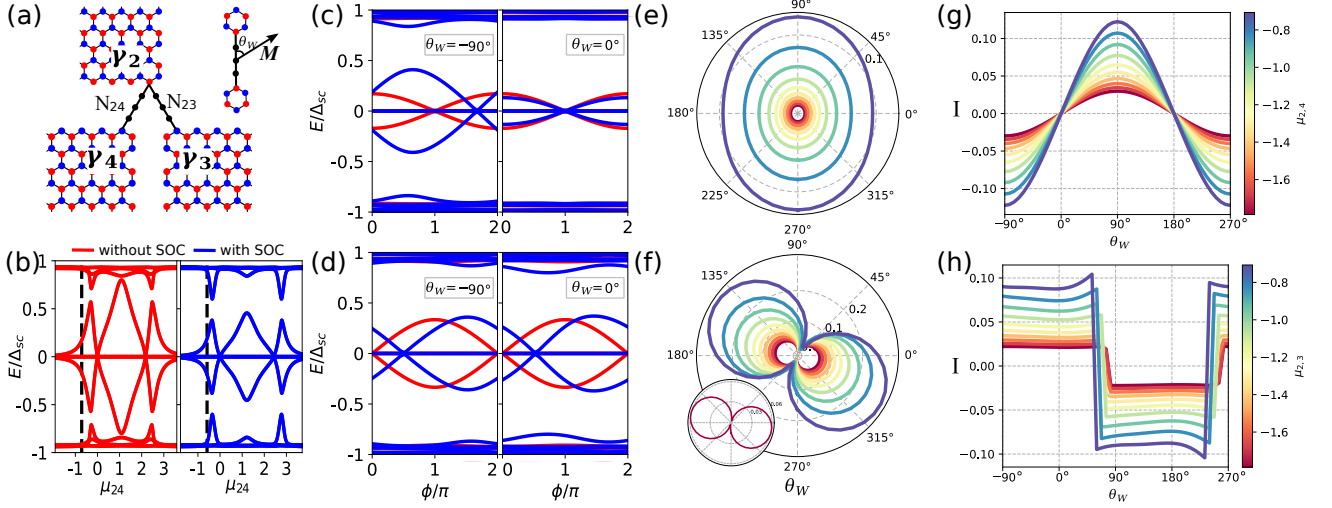


FIG. 3. (a) The configuration of the junction JJ_a and JJ_b , and θ_W is the angle between in-plane magnetic field \mathbf{M} and normal wire. (b) By fixing $\theta_W = -\pi/2$ and $\phi=0$, the red and blue curves are the energies change with chemical potential μ_{24} of the wires N_{24} without and with SOC JJ_a respectively. (c) Fixing chemical potential indicating by the black dot line in (b), the blue and red curves in the left and right figure, corresponding to $\theta_W = -\pi/2$ and 0 , are the Andreev spectrum of JJ_a in the case of normal wires without and with SOC respectively. (d) The left and the right figure are the Andreev spectrum of JJ_b at $\theta_W = -\pi/2$ and 0 , and the blue and red curves are representing the case of the wires without and with SOC. At $\phi=0$, (e)(f) are the dependence between Majorana couple and θ_W in JJ_a and JJ_b , (g)(h) are the dependence between between current and θ_W in JJ_a and JJ_b .

selective Andreev reflection when the polarization of ferromagnetic lead is perpendicular with the magnetic field direction. We still first set magnetic field \mathbf{M} to be along y direction while the spin orientation of the MCM, γ_1 , at B sublattice is along $-x$ direction (Fig. 1(a)). By attaching a ferromagnetic lead to the system (Fig. 2(a)) and varying the polarization of the lead, we calculate the finite-temperature conductance as[71]

$$G_T(V) = -\frac{2e^2}{\hbar} \int dE R(E) \frac{df(E-V)}{dE} \quad (5)$$

where V is the bias voltage, f is Fermi function and $R(E)$ is the probability of Andreev reflection obtaining from the transport package Kwant[72]. The conductance at finite temperature reaches a minimum when the lead polarization is along x direction, anti-parallel to the spin orientation of the MCMs without the lead. In this case, the lead has little effect on the orientation of MCMs (Fig 2(a)). When the lead polarization deviates from this direction, the spin orientation of the MCM is deflected (Fig 2(a)) while the conductance rises rapidly to the saturation value (Fig. 2(b)). It can be see more obviously in our plot of the lead polarization dependent ZBCP in the polar coordinate (blue curves in Fig. 2(c)). This is because the coupling between the spin-polarized lead and MCM break the local chiral symmetry and thus deflects the spin orientation of MCM (Fig. 2(a)), which further enhance the coupling between the MCM and the lead. When the system itself breaks the chiral symmetry, the spin texture is not strictly but still roughly perpendicular

to the direction of the magnetic field[71]. The lead polarization, corresponding to the minimal ZBCP, deviates from but is still close to x direction (the red curves in Fig. 2(c)). The high ZBCP shows similar behavior with that when the system respects chiral symmetry. Therefore, spin-selective Andreev reflection responds the applied magnetic field in the transverse direction, which is unique evidence for the MCMs in the class of HOTSC we are considering.

Majorana coupling and topological ϕ_0 -junction - Now, we consider two MCMs coupling through a normal lead (Fig. 3(a)) and associated Josephson effect. Here, the two MCMs come from different HOTSCs, which form topological Josephson junctions. Without loss of generality, we fix one MCM to be γ_2 , located at the right-bottom corner (Fig. 1(a)). When considering the normal wire without SOC and taking the magnetic field perpendicular to the normal wire, we plot the Andreev levels of the Josephson junction connecting γ_2 with γ_4 and γ_3 respectively (red curves in Fig. 3(c) and 3(d)). We find that the coupling between the two MCMs related by mirror operator, say $\gamma_2 - \gamma_4$, and inversion operator, say $\gamma_2 - \gamma_3$, gives topological 0-junction and π -junction with 4π periodicity respectively. For convenience, we call the Josephson junction for the former and the latter case as JJ_a and JJ_b . It has been shown that Majorana coupling is essential to perform fermion-parity measurements [73–75] and MZMs braiding [5, 76–80]. Meanwhile, fulfilling these tasks at $\phi = 0$ can suppress the disturbing signals

contributed from the possible topologically trivial channels. We then study the Majorana coupling magnitude at $\phi = 0$. For JJ_a , we plot the eigenenergies at $\phi = 0$ as a function of the chemical potential μ_{24} in the normal wire (in Fig. 3(b)). The Majorana coupling, indicated by the lowest positive eigenenergy, increases exponentially in the low chemical region and then oscillates with further increasing μ_{24} . Note that in the oscillation region, the coupling vanishes when μ_{24} across the eigenenergy of the isolated normal wire [27]. Along with the requirement to turn on and off the Majorana coupling exponentially accurate, we focus on the low μ_{24} region. For JJ_b , the Majorana coupling vanishes at $\phi = 0$ (red curves in Fig. 3(d)), which is protected by the inversion symmetry [71]. To open the Majorana coupling at $\phi = 0$ in the JJ_b , we add the Rashba SOC in the normal wire, which breaks the inversion symmetry and can be tuned by the electrical gate. The SOC shifts the Andreev crossing away from $\phi = 0$ and therefore opens the Majorana coupling in JJ_b (blue curves in Fig. 3(d)). Meanwhile, for JJ_a , the SOC also shifts the Andreev level crossing away from $\phi = \pi$ (blue curves in Fig. 3(c)). Obviously, this shift results in topological ϕ_0 -junction with finite Josephson current at $\phi = 0$. Here, as the existence of the MCMs does not depend on the in-plane magnetic field direction, we can study the Majorana coupling and associated Josephson current as a function of the magnetic field direction at $\phi = 0$, which remarkably show very different behavior in JJ_a and JJ_b . For JJ_a , the Majorana coupling only slightly depends on magnetic field direction (Fig. 3(e)). Meanwhile, the associated Josephson current amplitude oscillates with varying the angle between \mathbf{M} and the normal wire. Particularly the current vanishes under all μ_{24} values for \mathbf{M} parallel to the normal wire because the system restores the effective mirror symmetries in this case (Fig. 3(g)). For JJ_b , the Josephson coupling energy shows a strong \mathbf{M} direction dependence which also depends on μ_{23} . For very low μ_{23} , the junction has the maximal Majorana coupling when the magnetic field is close to parallel with the normal wire (Fig. 3(f)). With increasing μ_{23} , the maximal coupling direction starts to gradually shift to the direction with an angle of 45° to the normal wire. Meanwhile, the associated Josephson current remains insensitive to the magnetic field direction in a large angle range and switches direction when the magnetic field is in near parallel with the normal wire. These numerical results can be understood semi-quantitatively when we project the Josephson junction Hamiltonian in MCMs Hilbert space, which gives the Majorana coupling Hamiltonian at $\phi = 0$

$$\begin{aligned}\tilde{H}_{23} &= i\gamma_2\gamma_3\tilde{t}\sin\alpha_c\cos\frac{\beta}{2}, \\ \tilde{H}_{24} &= i\gamma_2\gamma_4\tilde{t}\cos(\theta_W + \alpha_c)\sin\frac{\beta}{2}\end{aligned}\quad (6)$$

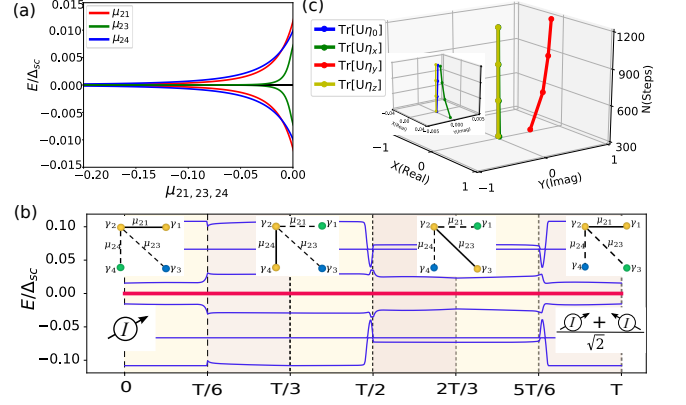


FIG. 4. (a) The relationship between chemical potential $\mu_{21}, \mu_{23}, \mu_{24}$ and the Majorana coupling magnitude respectively. (b) The energy spectrum in the whole procedure of exchanging γ_3 and γ_4 . The insets plot characterizes the exchange protocol of $\gamma_3 \leftrightarrow \gamma_4$. The ammeters indicate the Josephson current through N_d for the initial and final states of the braiding process. (c) The relationship between the coefficients (a_0, a_x, a_y, a_z) and the total steps.

and the associative Josephson current

$$\begin{aligned}I_{23} &= \frac{e\Delta}{\hbar} \sin\theta_W \sin\frac{\beta}{2}, \\ I_{24} &= \frac{e\Delta}{\hbar} \text{sgn}(\cos(\theta_W + \alpha_c)) \cos\frac{\beta}{2}.\end{aligned}\quad (7)$$

where $\beta = \delta kL$, and L is the length of the normal wire. Here, we assume the 1D Rashba SOC for simplicity [71]. It is clear that \tilde{H}_{23} does not explicitly depend on magnetic field direction while the associative Josephson current does vanish at $\theta_W = 0, \pi$ and reaches its maximal magnitude at $\theta_W = \pm\pi/2$. On the other hand, the Majorana coupling \tilde{H}_{24} does explicitly depend on θ_W which can explain the strong magnetic field direction dependence of the coupling magnitude. Meanwhile, the associative Josephson current remains a constant and only change sign when $\theta_W + \alpha_c$ across 0 or π . Note that $|\alpha_c|$ is larger when the coupling is stronger. The current switch deviates from the $\theta_W = \pm\pi/2$ more when the Majorana coupling is larger. These features are consistent with the numerical plot in Fig. 3(g)(h). Moreover, it is worth noting that the Majorana coupling induced Josephson current in JJ_a and JJ_b behave very differently with varying the magnetic field direction. Meanwhile, when the system is in the topological trivial regime, the combination of the magnetic field and SOC can in principle also induce ϕ_0 -junction [71]. However, we found the induced Josephson currents in both JJ_a and JJ_b are very small and behave qualitatively different from those in JJ_b [71]. Therefore, the observation of the ϕ_0 -junction in JJ_b can nevertheless provide a strong evidence for system entry into the topological region.

Now, we consider Majorana network shown in Fig. 1(b)

to braiding MCMs. The state is initialized by measuring the Josephson current direction through N_d . We then turn off the coupling between γ_3 and χ_1 and start to exchange the MCMs γ_3 and γ_4 by exponentially turning on and off the Majorana couplings through tuning the chemical potential in the region shown in Fig. 4(a). The whole process is divided into three intervals. In the first interval, we tune μ_{24} from 0 to μ_{24}^{\max} and μ_{21} from μ_{21}^{\max} to 0 so that the MCM at γ_4 position is moved to γ_1 position. In the second interval, we tune μ_{23} from 0 to μ_{23}^{\max} and μ_{24} from μ_{24}^{\max} to 0 so that the MCM at γ_3 position is moved to γ_4 position. At last, we change μ_{21} from 0 to μ_{21}^{\max} and μ_{23} from μ_{23}^{\max} to 0 so that the MCM at γ_1 position is moved to γ_3 position. During the braiding process, the energy of the two MZMs remains zero as indicated by the red line in Fig. 4(b) and separated from excited states by a finite energy gap. The non-abelian berry phase accumulated in the braiding process can be revealed through the path-ordered Wilson loop calculation in the MCMs basis $(\Psi_3(t), \Psi_4(t))^T$ [81–83]

$$\begin{aligned}
 U &= \mathcal{P}e^{-\oint d\mu A(t)} = \prod_{n=0}^{N-1} \sum_{\alpha, \beta=3}^4 \langle \Psi_\alpha(t_n) | \Psi_\beta(t_{n+1}) \rangle \\
 &= a_0 \eta_0 + a_x \eta_x + a_y \eta_y + a_z \eta_z,
 \end{aligned} \tag{8}$$

where $t_{n+1} - t_n = \Delta t = T/N$, N is the total steps for exchanging the MCMs in period T and η is Pauli matrix acting on the basis $(\Psi_3(0), \Psi_4(0))^T$. Our numerical calculation shows that the braiding matrix U has only η_y component whose amplitude approaches i with increasing the total steps N (Fig. 4(c)). This is consistent with the well know MZMs exchanging $\gamma_3 \rightarrow -\gamma_4$ and $\gamma_4 \rightarrow \gamma_3$ and renders the success of our all-electronically controlled braiding proposal. The experimental detection can be performed through measuring the Josephson current before and after the braiding. If the state is initialized by measuring the Josephson current direction through N_d , it will have 50% probability to observe the current direction switch after the successful MCMs braiding [71].

Conclusion - In conclusion, we provide a comprehensive scheme to detect and braiding MCMs in a class of HOTSC with the help of their unique spin properties. Our scheme is shown with the Kane-Mele model for realistic bismuthene but also valid for BHZ-model-base materials. The spin texture with the transverse polarization to the applied magnetic field leads to its spin-dependent transport qualitatively different from those in both the first-order TSC and topologically trivial superconducting states. This can provide the strong evidence that the system is in the HOTSC phase. We then propose an all electronically controlled Majorana network and numerically simulate the braiding process.

* jinhua@hust.edu.cn

† phyluxin@hust.edu.cn

- [1] D. A. Ivanov, *Phys. Rev. Lett.* **86**, 268 (2001).
- [2] A. Kitaev, *Annals of Physics* **303**, 2 (2003).
- [3] C. Nayak, S. H. Simon, A. Stern, M. Freedman, and S. Das Sarma, *Rev. Mod. Phys.* **80**, 1083 (2008).
- [4] J. Alicea, *75*, 076501 (2012).
- [5] C. Beenakker, *Annual Review of Condensed Matter Physics* **4**, 113 (2013).
- [6] S. D. Sarma, M. Freedman, and C. Nayak, *npj Quantum Information* **1**, 15001 (2015).
- [7] S. R. Elliott and M. Franz, *Rev. Mod. Phys.* **87**, 137 (2015).
- [8] F. Pientka, G. Kells, A. Romito, P. W. Brouwer, and F. von Oppen, *Phys. Rev. Lett.* **109**, 227006 (2012).
- [9] J. Liu, A. C. Potter, K. T. Law, and P. A. Lee, *Phys. Rev. Lett.* **109**, 267002 (2012).
- [10] W. S. Cole, J. D. Sau, and S. Das Sarma, *Phys. Rev. B* **94**, 140505 (2016).
- [11] C.-X. Liu, J. D. Sau, T. D. Stanescu, and S. Das Sarma, *Phys. Rev. B* **96**, 075161 (2017).
- [12] S. Das Sarma and H. Pan, *Phys. Rev. B* **103**, 195158 (2021).
- [13] H. Pan, C.-X. Liu, M. Wimmer, and S. Das Sarma, *Phys. Rev. B* **103**, 214502 (2021).
- [14] H. Pan and S. Das Sarma, *Phys. Rev. B* **104**, 054510 (2021).
- [15] D. Sticlet, C. Bena, and P. Simon, *Phys. Rev. Lett.* **108**, 096802 (2012).
- [16] J. J. He, T. K. Ng, P. A. Lee, and K. T. Law, *Phys. Rev. Lett.* **112**, 037001 (2014).
- [17] H.-H. Sun, K.-W. Zhang, L.-H. Hu, C. Li, G.-Y. Wang, H.-Y. Ma, Z.-A. Xu, C.-L. Gao, D.-D. Guan, Y.-Y. Li, C. Liu, D. Qian, Y. Zhou, L. Fu, S.-C. Li, F.-C. Zhang, and J.-F. Jia, *Phys. Rev. Lett.* **116**, 257003 (2016).
- [18] M. Serina, D. Loss, and J. Klinovaja, *Phys. Rev. B* **98**, 035419 (2018).
- [19] S. Głodzik, N. Sedlmayr, and T. Domański, *Phys. Rev. B* **102**, 085411 (2020).
- [20] Y. Asano and Y. Tanaka, *Phys. Rev. B* **87**, 104513 (2013).
- [21] H. Ebisu, K. Yada, H. Kasai, and Y. Tanaka, *Phys. Rev. B* **91**, 054518 (2015).
- [22] X. Liu, J. D. Sau, and S. Das Sarma, *Phys. Rev. B* **92**, 014513 (2015).
- [23] K. Zhang, J. Zeng, Y. Ren, and Z. Qiao, *Phys. Rev. B* **96**, 085117 (2017).
- [24] L. Chen, Y.-H. Wu, and X. Liu, *Phys. Rev. B* **99**, 165307 (2019).
- [25] R. M. Lutchyn, J. D. Sau, and S. Das Sarma, *Phys. Rev. Lett.* **105**, 077001 (2010).
- [26] D. M. Badiane, M. Houzet, and J. S. Meyer, *Phys. Rev. Lett.* **107**, 177002 (2011).
- [27] X. Liu, X. Li, D.-L. Deng, X.-J. Liu, and S. Das Sarma, *Phys. Rev. B* **94**, 014511 (2016).
- [28] M. Guigou, N. Sedlmayr, J. M. Aguiar-Hualde, and C. Bena, **115**, 47005 (2016).
- [29] E. Prada, R. Aguado, and P. San-Jose, *Phys. Rev. B* **96**, 085418 (2017).
- [30] A. A. Aligia, D. Pérez Daroca, and L. Arrachea, *Phys. Rev. Lett.* **125**, 256801 (2020).

- [31] J. Alicea, Y. Oreg, G. Refael, F. von Oppen, and M. P. A. Fisher, *Nature Physics* **7**, 412 (2011).
- [32] B. van Heck, A. R. Akhmerov, F. Hassler, M. Burrello, and C. W. J. Beenakker, **14**, 035019 (2012).
- [33] X.-J. Liu, C. L. M. Wong, and K. T. Law, *Phys. Rev. X* **4**, 021018 (2014).
- [34] A. Stern and E. Berg, *Phys. Rev. Lett.* **122**, 107701 (2019).
- [35] S. Vijay and L. Fu, *Phys. Rev. B* **94**, 235446 (2016).
- [36] J. Langbehn, Y. Peng, L. Trifunovic, F. von Oppen, and P. W. Brouwer, *Phys. Rev. Lett.* **119**, 246401 (2017).
- [37] Z. Yan, F. Song, and Z. Wang, *Phys. Rev. Lett.* **121**, 096803 (2018).
- [38] Y. Wang, M. Lin, and T. L. Hughes, *Phys. Rev. B* **98**, 165144 (2018).
- [39] Q. Wang, C.-C. Liu, Y.-M. Lu, and F. Zhang, *Phys. Rev. Lett.* **121**, 186801 (2018).
- [40] C.-H. Hsu, P. Stano, J. Klinovaja, and D. Loss, *Phys. Rev. Lett.* **121**, 196801 (2018).
- [41] T. Liu, J. J. He, and F. Nori, *Phys. Rev. B* **98**, 245413 (2018).
- [42] Y. Volpez, D. Loss, and J. Klinovaja, *Phys. Rev. Lett.* **122**, 126402 (2019).
- [43] R.-X. Zhang, W. S. Cole, and S. Das Sarma, *Phys. Rev. Lett.* **122**, 187001 (2019).
- [44] X. Zhu, *Phys. Rev. Lett.* **122**, 236401 (2019).
- [45] M. Ezawa, *Phys. Rev. B* **100**, 045407 (2019).
- [46] S. A. A. Ghorashi, X. Hu, T. L. Hughes, and E. Rossi, *Phys. Rev. B* **100**, 020509 (2019).
- [47] S. Franca, D. V. Efremov, and I. C. Fulga, *Phys. Rev. B* **100**, 075415 (2019).
- [48] X.-H. Pan, K.-J. Yang, L. Chen, G. Xu, C.-X. Liu, and X. Liu, *Phys. Rev. Lett.* **123**, 156801 (2019).
- [49] R.-X. Zhang, W. S. Cole, X. Wu, and S. Das Sarma, *Phys. Rev. Lett.* **123**, 167001 (2019).
- [50] Z. Yan, *Phys. Rev. Lett.* **123**, 177001 (2019).
- [51] Z. Yan, *Phys. Rev. B* **100**, 205406 (2019).
- [52] A. Tiwari, M.-H. Li, B. A. Bernevig, T. Neupert, and S. A. Parameswaran, *Phys. Rev. Lett.* **124**, 046801 (2020).
- [53] Y.-J. Wu, J. Hou, Y.-M. Li, X.-W. Luo, X. Shi, and C. Zhang, *Phys. Rev. Lett.* **124**, 227001 (2020).
- [54] S. A. A. Ghorashi, T. L. Hughes, and E. Rossi, *Phys. Rev. Lett.* **125**, 037001 (2020).
- [55] S.-B. Zhang, A. Calzona, and B. Trauzettel, *Phys. Rev. B* **102**, 100503 (2020).
- [56] S.-B. Zhang, W. B. Rui, A. Calzona, S.-J. Choi, A. P. Schnyder, and B. Trauzettel, *Phys. Rev. Research* **2**, 043025 (2020).
- [57] Y.-X. Li and T. Zhou, *Phys. Rev. B* **103**, 024517 (2021).
- [58] A. K. Ghosh, T. Nag, and A. Saha, *Phys. Rev. B* **103**, 045424 (2021).
- [59] A. K. Ghosh, T. Nag, and A. Saha, *Phys. Rev. B* **103**, 085413 (2021).
- [60] B.-X. Li and Z. Yan, *Phys. Rev. B* **103**, 064512 (2021).
- [61] L. Chen, B. Liu, G. Xu, and X. Liu, *Phys. Rev. Research* **3**, 023166 (2021).
- [62] J. Niu, T. Yan, Y. Zhou, Z. Tao, X. Li, W. Liu, L. Zhang, H. Jia, S. Liu, Z. Yan, Y. Chen, and D. Yu, *Science Bulletin* **66**, 1168 (2021).
- [63] X.-J. Luo, X.-H. Pan, and X. Liu, *Phys. Rev. B* **104**, 104510 (2021).
- [64] G. Li, W. Hanke, E. M. Hankiewicz, F. Reis, J. Schäfer, R. Claessen, C. Wu, and R. Thomale, *Phys. Rev. B* **98**, 165146 (2018).
- [65] G.-F. Zhang, Y. Li, and C. Wu, *Phys. Rev. B* **90**, 075114 (2014).
- [66] F. Reis, G. Li, L. Dudy, M. Bauernfeind, S. Glass, W. Hanke, R. Thomale, J. Schäfer, and R. Claessen, *Science* **357**, 287 (2021).
- [67] C. L. Kane and E. J. Mele, *Phys. Rev. Lett.* **95**, 146802 (2005).
- [68] C. L. Kane and E. J. Mele, *Phys. Rev. Lett.* **95**, 226801 (2005).
- [69] B. B. Andrei, L. Hughes Taylor, and Z. Shou-Cheng, *Science* **314**, 1757 (2021).
- [70] X.-L. Qi and S.-C. Zhang, *Rev. Mod. Phys.* **83**, 1057 (2011).
- [71] Supplemental material for the following: I. Spin texture. II spin selective zero bias conductance peak. III ϕ_0 josephson junction. IV. Similar spin texture and transport properties in BHZ model.
- [72] C. W. Groth, M. Wimmer, A. R. Akhmerov, and X. Waintal, *New Journal of Physics* **16**, 063065 (2014).
- [73] S. Vijay and L. Fu, *Phys. Rev. B* **94**, 235446 (2016).
- [74] T. Karzig, C. Knapp, R. M. Lutchyn, P. Bonderson, M. B. Hastings, C. Nayak, J. Alicea, K. Flensberg, S. Plugge, Y. Oreg, C. M. Marcus, and M. H. Freedman, *Phys. Rev. B* **95**, 235305 (2017).
- [75] D. Litinski and F. von Oppen, *Phys. Rev. B* **96**, 205413 (2017).
- [76] J. D. Sau, D. J. Clarke, and S. Tewari, *Phys. Rev. B* **84**, 094505 (2011).
- [77] D. Pekker, C.-Y. Hou, V. E. Manucharyan, and E. Demler, *Phys. Rev. Lett.* **111**, 107007 (2013).
- [78] B. van Heck, T. Hyart, and C. W. J. Beenakker, *Physica Scripta* **T164**, 014007 (2015).
- [79] D. Aasen, M. Hell, R. V. Mishmash, A. Higginbotham, J. Danon, M. Leijnse, T. S. Jespersen, J. A. Folk, C. M. Marcus, K. Flensberg, and J. Alicea, *Phys. Rev. X* **6**, 031016 (2016).
- [80] J. P. T. Stenger, M. Hatridge, S. M. Frolov, and D. Pekker, *Phys. Rev. B* **99**, 035307 (2019).
- [81] F. Wilczek and A. Zee, *Phys. Rev. Lett.* **52**, 2111 (1984).
- [82] R. Yu, X. L. Qi, A. Bernevig, Z. Fang, and X. Dai, *Phys. Rev. B* **84**, 075119 (2011).
- [83] K. Snizhko, R. Egger, and Y. Gefen, *Phys. Rev. Lett.* **123**, 060405 (2019).